

Temporal and Spectral Variabilities of High Energy Emission from Blazars Using Synchrotron Self-Compton Models

Hui Li¹ and Masaaki Kusunose²

ABSTRACT

Multiwavelength observations of blazars such as Mrk 421 and Mrk 501 show that they exhibit strong short time variabilities in flare-like phenomena. Based on the homogeneous synchrotron self-Compton (SSC) model and assuming that time variability of the emission is initiated by changes in the injection of nonthermal electrons, we perform detailed temporal and spectral studies of a purely cooling plasma system, using parameters appropriate to blazars. One important parameter is the total injected energy \mathcal{E} and we show how the synchrotron and Compton components respond as \mathcal{E} varies. When the synchrotron and SSC components have comparable peak fluxes, we find that the SSC process contributes strongly to the electron cooling and the whole system is nonlinear, thus simultaneously solving electron and photon kinetic equations is necessary. In the limit of the injection-dominated situation when the cooling timescale is long, we find a unique set of model parameters that are fully constrained by observable quantities. In the limit of cooling-dominated situation, TeV emissions arise mostly from a cooled electron distribution and Compton scattering process is always in the Klein-Nishina regime, which makes the TeV spectrum having a large curvature. Furthermore, even in a single injection event, the multiwavelength light-curves do not necessarily track each other because the electrons that are responsible for those emissions might have quite different lifetimes. We discuss in detail how one could infer important physical parameters using the observed spectra. In particular, we could infer the size of the emission region by looking for exponential decay in the light curves. We could also test the basic assumption of SSC by measuring the difference in the rate of peak energy changes of synchrotron and SSC peaks. We also show that the trajectory in the photon-index-flux plane evolves clockwise or counter-clockwise depending on the value of \mathcal{E} and observed energy bands.

Subject headings: BL Lacertae objects: general – gamma rays: theory – radiation mechanisms: nonthermal

¹Theoretical Astrophysics (T-6, MS B288), Los Alamos National Laboratory, Los Alamos, NM 87545; hli@lanl.gov

²Department of Physics, School of Science, Kwansei Gakuin University, Nishinomiya 662-8501, Japan; kusunose@kwansei.ac.jp

1. INTRODUCTION

Blazars are a class of flat radio spectrum, core-dominated active galactic nuclei (AGNs). The overall radiation spectra of blazars show two broad peaks in the νF_ν space; one is between IR and X-rays, and the other in the γ -ray regime (e.g., von Montigny et al. 1995). Flares also have been observed at X- and gamma-ray bands by multiwavelength observations of Mrk 421 (e.g., Macomb et al. 1995; Macomb et al. 1996 for erratum; Buckley et al. 1996) and Mrk 501 (Catanese et al. 1997; Pian et al. 1998). The tremendous luminosity and fast time variabilities from blazars have led to the usual arguments that relativistic motion is occurring in the emitting plasma. Moreover, the favored scenario to explain these sources is that we are viewing nearly along the axis of a relativistically outflowing plasma jet that has been ejected from an accreting super massive black hole (e.g., Blandford & Rees 1978).

Although the origin of these multiwavelength spectra is still under debate, several models on the radiative processes have been put forth, in particular, models of Compton scattering of synchrotron photons or external photons have been developed in recent years (e.g., Bloom & Marscher 1996; Inoue & Takahara 1996; Ghisellini & Madau 1996; Dermer, Sturmer, & Schlickeiser 1997; Mastichiadis & Kirk 1997; Sikora et al. 1997; Böttcher, Mause, & Schlickeiser 1997; Georganopoulos & Marscher 1998; Ghisellini et al. 1998). Most of these calculations are either semi-analytic, or for steady state situations, or not including the Compton scattering process self-consistently. The main purpose of this paper is to improve upon this situation. The physics of how energy is dissipated into relativistic particles is, unfortunately, not well understood (see, however, Romanova & Lovelace 1997) and will not be treated fully in this paper.

Among various blazar models, synchrotron self-Compton (SSC) models have received a fair amount of attention, by virtue of its simplicity and its possible predictive power. In these models, it is proposed that the nonthermal synchrotron emission forms the radio-through-X-ray continuum, and that the Compton scattering of these (soft) synchrotron photons by the same nonthermal electrons produces the gamma rays (\sim GeV – TeVs). In this paper, we focus on the so-called homogeneous SSC model where a spherical blob of uniform relativistic plasma is postulated. Even with such a greatly simplified picture, a number of parameters have to be invoked, whose interplay gives rise to a rich dynamic behavior of the observed radiation. Of particular interest is the correlated variabilities in X-ray and γ -ray fluxes, since they represent the tail of nonthermal electrons which have the shortest cooling timescale. Although the generic multiwavelength spectra from radio to TeV can be fitted by a steady state model with fixed parameters (e.g, Kataoka et al. 1999), time-dependent calculations almost always offer stronger constraints. Furthermore, when the self-Compton component contains a comparable or even larger fraction of the radiative energy than the synchrotron component, the whole problem becomes inherently nonlinear and both components need to be calculated simultaneously and self-consistently. This naturally leads to the need of solving coupled, time-dependent, nonlinear particle and photon kinetic-equations. Moreover, by examining the energy-dependence of flare data at gamma-ray energies, one could potentially discriminate between SSC and external Compton-scattering origins of the seed photons

(Dermer 1998).

The simplest model for time variability of blazars (Mastichiadis & Kirk 1997; hereafter MK97) assumes that electrons obeying a power-law distribution are injected uniformly throughout a relativistically moving blob over an extended period of time, and that electrons cool by both synchrotron radiation and Compton scattering. The blob is assumed not to accelerate or decelerate, and the energy loss by Compton scattering of photons impinging from outside the blob is assumed to be small in comparison with the synchrotron self-Compton loss. MK97 reproduced the qualitative behavior of the energy-dependent lags and the hysteresis diagrams (Takahashi et al. 1996). Much of the work presented here follows closely to the previous study by MK97, but we are using a completely different kinetic code which will be discussed in later sections. Kirk, Rieger, & Mastichiadis (1998) further modeled the evolution of synchrotron emission, calculating acceleration and cooling regions separately, though Compton scattering was not included.

In this paper we present a detailed study of the time-evolution of an electron-photon plasma (the positive particles could be either protons or positrons) by solving the kinetic equations numerically. We briefly describe our model in §2 and show numerical results in §3. Summary is given in §4.

2. MODEL

We assume that observed photons are emitted from a blob moving relativistically towards us with a Doppler factor $\mathcal{D} = [\Gamma(1 - \beta_\Gamma \cos \theta)]^{-1}$, where Γ is the Lorentz factor of the blob, $\beta_\Gamma c$ is the velocity with c being the light speed, and θ is the angle between the direction of blob motion and the line of sight. The blob is a spherical and uniform cloud with radius R . Relativistic electrons are injected into the blob and produce high energy emission. Electrons and photons are uniformly distributed throughout the blob. The most important physical processes for electrons include synchrotron radiation and Compton scattering. The spectra of electrons and photons in the blob are calculated by solving the kinetic equations described below (see also Coppi & Blandford 1990).

The kinetic equation describing the time-evolution of electron distribution $n(\gamma)$ is given by

$$\frac{\partial n}{\partial t} = -\frac{\partial}{\partial \gamma} \left[\left(\frac{d\gamma}{dt} \right)_{\text{loss}} n \right] + \frac{1}{2} \frac{\partial^2}{\partial \gamma^2} (D_e n) - \frac{n}{t_{e,\text{esc}}} + Q(\gamma), \quad (1)$$

where n is the electron number density per γ , γ is the electron Lorentz factor, and $t_{e,\text{esc}}$ is the time for electrons to escape from the blob. The term $(d\gamma/dt)_{\text{loss}}$ represents various electron energy loss processes, such as synchrotron and Compton scattering; their corresponding energy diffusion is given as D_e . We also include the synchrotron “boiler” effect (Ghisellini et al. 1988) and other processes such as Coulomb collisions, though they are not important in the present study. Pair-production and annihilation are not treated in the present code, though they tend to be less important too. In our code, the particle equation is actually discretized in the momentum space so that thermal particles and their processes can be handled accurately. This is less important for

AGN jet parameters but will be very useful for modeling the emissions from stellar-mass black hole systems. Note that equation (1) assumes a continuous electron energy loss (i.e., Fokker-Planck type). This assumption does not account for the situation when there is a significant energy loss in a single Compton scattering which is important in the Klein-Nishina regime. This discrete nature of the Compton energy loss is, however, included in the photon kinetic equation, i.e., equations (2) and (3). We have checked the accuracy of the continuous approximation of the Compton energy loss in equation (1) in view of energy conservation. Our numerical tests show that the total energy is conserved with the accuracy better than 5 per cent after 10 R/c , when the SSC component is dominant and the scatterings occur frequently in the Klein-Nishina regime.

The relevant kinetic equation for the time-evolution of photons is given by

$$\frac{\partial n_{\text{ph}}(\epsilon)}{\partial t} = \dot{n}_{\text{C}}(\epsilon) + \dot{n}_{\text{em}}(\epsilon) - \dot{n}_{\text{abs}}(\epsilon) - \frac{n_{\text{ph}}(\epsilon)}{t_{\text{ph,esc}}}, \quad (2)$$

where $n_{\text{ph}}(\epsilon)$ is the photon number spectrum per unit volume per unit energy ϵ . Compton scattering is calculated as

$$\dot{n}_{\text{C}}(\epsilon) = -n_{\text{ph}}(\epsilon) \int d\gamma n(\gamma) R_{\text{C}}(\epsilon, \gamma) + \int \int d\epsilon' d\gamma P(\epsilon; \epsilon', \gamma) R_{\text{C}}(\epsilon', \gamma) n_{\text{ph}}(\epsilon') n(\gamma). \quad (3)$$

First term of the right hand side of equation (3) denotes the rate that photons with energy ϵ are scattered by electrons with number spectrum $n(\gamma)$ per unit volume per unit γ ; R_{C} is the angle-averaged scattering rate. Second term of equation (3) denotes the spectrum of scattered photons: $P(\epsilon; \epsilon', \gamma)$ is the probability that a photon with energy ϵ' is scattered off by an electron with γ to have energy ϵ . The probability P is normalized such that $\int P(\epsilon; \epsilon', \gamma) d\epsilon = 1$. The details of R_{C} and P are given in Jones (1968) and the appendix A of Coppi & Blandford (1990). We use the exact Klein-Nishina cross section in the calculations of Compton scattering. Photon production and self-absorption by synchrotron radiation are included in $\dot{n}_{\text{em}}(\epsilon)$ and $\dot{n}_{\text{abs}}(\epsilon)$, respectively. The synchrotron emissivity and the absorption coefficient are calculated using the approximations given in Robinson and Melrose (1984) for transrelativistic electrons and Crusius and Schlickeiser (1986) for relativistic electrons. External photon sources such as disk photons can be included, though they are not considered here. The rate of photon escape is estimated as $n_{\text{ph}}(\epsilon)/t_{\text{ph,esc}}$. Since we are in the optically thin limit, we set $t_{\text{ph,esc}} = R/c$, which is a good approximation. The photon spectra from solving equation (2) has been extensively compared with those from Monte-Carlo simulations and we have found very good agreement between them (Kusunose, Coppi, & Li 1999).

The comoving quantities are transformed back into the observer's frame using $\epsilon_{\text{obs}} = \epsilon \mathcal{D}/(1+z)$ and $dt_{\text{obs}} = dt(1+z)/\mathcal{D}$, where z is the redshift of the source.

We assume that electrons are injected obeying a power law in energy:

$$Q(\gamma, t) = Q_0(t) \gamma^{-p}$$

with $\gamma_{\text{min}} \leq \gamma \leq \gamma_{\text{max}}$. The total energetics of the electrons can be represented by a compactness parameter which is proportional to L/R , where L is the source luminosity. We do not consider

specific acceleration mechanisms in this paper. Thus particles are just being injected into the blob over a finite time. We emphasize that in order to be consistent with the basic assumption of spatial homogeneity, we require the injection time t_{inj} to be longer than $t_{\text{dyn}} = R/c$. In effect, we can not probe variabilities shorter than t_{dyn} in the comoving frame. Other physical effects such as adiabatic loss via expansion might play an important role but is not considered here. It is unfortunate that we need such a large number of parameters to proceed with the calculations, and this is the main reason we opt not to add further complications such as acceleration.

3. RESULTS

The dynamic behavior of the emission spectra is controlled by several timescales, namely, the cooling time t_{cool} , the dynamic time t_{dyn} , the injection duration t_{inj} , and the escape time t_{esc} . The causality argument requires that $t_{\text{dyn}} \leq t_{\text{inj}}, t_{\text{esc}}$, whereas t_{cool} can be smaller than t_{dyn} . For SSC models, both synchrotron and Compton processes contribute to the electron cooling, so $1/t_{\text{cool}} = 1/t_{\text{syn}} + 1/t_{\text{ssc}}$, where $t_{\text{syn}} = \gamma/|\dot{\gamma}_{\text{syn}}|$ and $t_{\text{ssc}} = \gamma/|\dot{\gamma}_{\text{ssc}}|$.

In the following analyses, we will divide our results into two major parts, based on whether t_{cool} is longer or shorter than t_{inj} . In the limit of $t_{\text{cool}} \geq t_{\text{inj}} \geq t_{\text{dyn}}$, where t_{cool} is evaluated using the highest particle energy, the injected particle distribution does not change appreciably during the injection process. We call this the injection-dominated limit. On the other hand, if $t_{\text{inj}} \geq t_{\text{dyn}} \geq t_{\text{cool}}$, then particles will be sufficiently cooled while the injection still occurs, and emissions are from a cooled particle distribution rather than from the injected one. We call this the cooling-dominated limit. Consequently, we expect rapid variations in both fluxes and spectra in the latter case and relatively slow spectral variations in the former case.

The primary purpose of this paper is to understand the dynamics of SSC model. We thus have chosen a broad range of parameters rather than try to fit any specific source spectrum, but we certainly use parameters thought to be applicable to those sources (Mrk 421 in particular) to guide our calculations.

3.1. Long Cooling Time Limit

We show that, in this limit, a set of SSC model parameters can be uniquely determined from the observable quantities. We use observations of Mrk 421 as an example and further discuss their implications for multiwavelength observations.

3.1.1. A Unique Solution

Let \mathcal{E} represent the energy (in ergs) injected in nonthermal electrons, which we assume can be described as $N_e(\gamma) = N_0 \gamma^{-p}$ and $\gamma_{\min} \leq \gamma \leq \gamma_{\max}$. Then $N_0 = (2 - p)\mathcal{E}/[m_e c^2(\gamma_{\max}^{2-p} - \gamma_{\min}^{2-p})]$ (for $p \neq 2$). In the limit of long cooling time, we can use the injected electron distribution to calculate the synchrotron and SSC fluxes. Thus, for the peak energies of synchrotron and SSC, we have

$$\mathcal{D}\gamma_{\max}^2 B \approx \nu_{\text{syn}}/2.8 \times 10^6 = \tilde{\nu}_{\text{syn}} \quad , \quad (4)$$

$$\mathcal{D}\gamma_{\max} \approx \nu_{\text{ssc}}/1.236 \times 10^{20} = \tilde{\nu}_{\text{ssc}} \quad , \quad (5)$$

where ν_{syn} and ν_{ssc} are the synchrotron and γ -ray peaks in Hz, respectively, and B is magnetic fields in Gauss. The numerical normalization factors are easily obtainable using the standard expressions for the peak synchrotron energy and inverse Compton peak energy in the KN limit. For Mrk 421, we have $\tilde{\nu}_{\text{syn}} \approx 1.72 \times 10^{11}$ (~ 2 keV) and $\tilde{\nu}_{\text{ssc}} \approx 10^7$ (~ 5 TeV). From equations (4) and (5), we get

$$B = \mathcal{D}\tilde{\nu}_{\text{syn}}/\tilde{\nu}_{\text{ssc}}^2 \quad . \quad (6)$$

The relative ratio η of SSC to synchrotron fluxes for Mrk 421 is close to 1. This ratio can be approximately represented by the ratio of the comoving-frame synchrotron photon energy-density, $U_{\text{syn}} = L_{\text{syn}}/(4\pi R^2 c \mathcal{D}^4)$, to the magnetic field energy-density, $U_B = B^2/(8\pi)$. But the exact value of η could be quite different from this estimate owing to several factors: the end point effect at the peak of both synchrotron and SSC fluxes,³ the KN effect of Compton scattering for producing TeV emission, and the fact that the electron distribution will be slightly cooled even though the cooling timescale is long. It is very difficult to get an exact analytic value to account for all these effects, so we introduce a correction factor f_c in calculating η . Thus, we have

$$\eta = f_c \frac{U_{\text{syn}}}{U_B} \quad \text{or} \quad L_{\text{syn}} \approx \mathcal{D}^4 4\pi R^2 c U_B (\eta/f_c) \quad . \quad (7)$$

Furthermore, since all blazar sources are observed to be highly variable, an additional constraint has usually been proposed that

$$R \approx \mathcal{D} ct_{\text{var}} \quad , \quad (8)$$

where t_{var} is defined as a variability timescale in the observer's frame.

Combining all the equations given above, we have 4 equations for 4 independent variables (i.e., \mathcal{D} , B , γ_{\max} , and R). The supplemental information include $\tilde{\nu}_{\text{syn}}$, $\tilde{\nu}_{\text{ssc}}$, L_{syn} , η , and t_{var} , with a

³For $p < 3$, the peak of νL_ν is at $\nu_{\text{syn}} \propto \gamma_{\max}^2 B$, but its flux is *smaller* than that obtained using the δ -function approximation to the scattering cross section. To be consistent with our numerical code results which have used the *exact* synchrotron emissivity formulations, we have introduced a reduction factor of $f_{\text{syn}} (< 1)$ in our simplified analytic estimates for the peak synchrotron flux (see also equation (10)). Note that this reduction only applies to the end points of emissivity. For energies much smaller than ν_{syn} , the δ -function approximation is quite accurate.

somewhat variable factor f_c . Thus we can *uniquely* determine a solution set for all the parameters. The Doppler factor from this solution (denoted by a subscript ‘s’) can be expressed as

$$\mathcal{D}_s \approx 22.2 \left(\frac{L_{\text{syn}}}{6 \times 10^{44}} \right)^{\frac{1}{8}} \left(\frac{\tilde{\nu}_{\text{SSC}}}{10^7} \right)^{\frac{1}{2}} \left(\frac{\tilde{\nu}_{\text{syn}}}{1.7 \times 10^{11}} \right)^{-\frac{1}{4}} \left(\frac{t_{\text{var}}}{10^4} \right)^{-\frac{1}{4}} \left(\frac{f_c}{0.4} \right)^{\frac{1}{8}} \left(\frac{\eta}{1.0} \right)^{-\frac{1}{8}} . \quad (9)$$

The peak luminosity (L_{syn}) of the synchrotron component in the observer’s frame can be estimated using νL_ν at ν_{syn} (again taking into account the end-point effects),

$$L_{\text{syn}} \approx \mathcal{D}^4 f_{\text{syn}} \frac{2(2-p)}{3} \sigma_{\text{T}} c U_B \frac{\mathcal{E}}{m_e c^2} \gamma_{\text{max}} , \quad (10)$$

where σ_{T} is the Thomson cross section, $f_{\text{syn}} (< 1)$ represents the reduction of synchrotron flux at the end point, \mathcal{D}^4 is due to the Doppler boosting. Observationally, L_{syn} at ~ 2 keV is $\geq 6 \times 10^{44}$ ergs s^{-1} with a luminosity distance of 3.8×10^{26} cm ($z = 0.0308$) for a $q_0 = 1/2$ and $\Lambda = 0$ cosmology. Here, $H_0 = 75$ km s^{-1} Mpc $^{-1}$ is assumed. Also, fitting of Mrk 421’s synchrotron spectrum suggests $p \approx 1.65$ (MK97). From this, we can determine the rest of the parameters for this unique solution (again denoted by a subscript ‘s’)

$$B_s = \mathcal{D}_s \tilde{\nu}_{\text{syn}} / \tilde{\nu}_{\text{SSC}}^2 \approx 0.038 \text{ G} , \quad (11)$$

$$\gamma_{\text{max},s} = \tilde{\nu}_{\text{SSC}} / \mathcal{D}_s \approx 4.5 \times 10^5 , \quad (12)$$

$$R_s = c t_{\text{var}} \mathcal{D}_s \approx 6.5 \times 10^{15} \text{ cm} , \quad (13)$$

$$\mathcal{E}_s = \frac{1.55 \times 10^9}{(2-p) f_{\text{syn}}} \frac{L_{\text{syn}}}{\gamma_{\text{max},s} B_s^2 \mathcal{D}_s^4} \approx 4.1 \times 10^{46} \text{ ergs} , \quad (14)$$

where we have used $p = 1.65$ and $f_{\text{syn}} = 0.4$.⁴ More importantly, we can check our original assumption that cooling time is long compared to $t_{\text{dyn}} = R/c$. This is obviously satisfied since $t_{\text{syn}} \approx (6\pi m_e c / \sigma_{\text{T}}) / (\gamma_{\text{max}} B^2) \approx 1.2 \times 10^6$ sec, which is much longer than $t_{\text{dyn}} \approx 2.2 \times 10^5$ sec.

Using the above derived parameters, we solve equations (1) and (2) simultaneously and follow the evolution until $20t_{\text{dyn}}$. A total energy of \mathcal{E} is injected in nonthermal electrons over a comoving timescale of $t_{\text{inj}} = 2t_{\text{dyn}}$. In these calculations electrons are not allowed to escape. Figure 1 shows the time evolution of electron and photon distributions as the system evolves. Note that the time for synchrotron and SSC components to reach their peak fluxes is different, and that it happens after the electron injection has stopped. To qualitatively understand this, we can write the photon kinetic equation symbolically as

$$\frac{\partial n_{\text{ph}}(\epsilon)}{\partial t} = \text{Production}(\epsilon) - \text{Escape}(\epsilon) . \quad (15)$$

⁴The fact that f_c and f_{syn} are both chosen as 0.4 is a coincidence. The evaluation of f_c involves end-point effects from both synchrotron and Compton scattering, whereas f_{syn} is only concerned with synchrotron. The value 0.4 is obtained by comparing the analytic estimates with the exact numerical calculations.

Thus, the photon flux at energy ϵ will increase if the production rate is larger than the escape and decrease if escape is quicker. This determines when the peak of photon flux at certain energy is reached. Using photon flux at keV as an example, the production of these photons still continues even when the electron injection stops because the cooling timescale is much longer than R/c . Eventually as electrons cool, they can no longer produce keV synchrotron emissions, the flux at keV starts to decline.

Figure 2 shows the light curves at different energy bands expected from this injection event. Since the cooling time is rather long, only the energy bands corresponding to the tail of electron distributions show short time variabilities due to that electron injection is turned on and off; whereas other energy bands show a long plateau, representing a balance between the photon production and escape. A clear prediction from this is that there should be very little spectral evolution except at the peaks of synchrotron and SSC. All these are commensurate with the dynamics of electron cooling.

In order to further differentiate the role of synchrotron versus Compton cooling on electrons, we plot the ratio of $|\dot{\gamma}_{\text{ssc}}/\dot{\gamma}_{\text{syn}}|$ as a function of electron energies at different times in Figure 3. It is clear that SSC cooling becomes more important than synchrotron cooling when the photon energy density builds up within the system as time proceeds. After reaching the peak, the SSC cooling starts to decrease as the photon energy density decreases. The dependence of this ratio on the electron energy is partly due to the KN effect. This figure clearly indicates that one can not ignore SSC cooling in estimating certain parameters and that the evolution is very nonlinear, thus a self-consistent numerical calculation is required for fitting the data more accurately.

Note that the spectra given in Figure 1 is not intended to be an accurate fit to the observed spectra from Mrk 421. In fact, the TeV spectrum of Mrk 421 is known to be roughly a power law (Krennrich et al. 1999), but the generic spectrum in TeV obtained here has a clear curvature, due to the fact that the Compton scattering is in the KN regime. Nevertheless, this exercise allows us to establish a parameter space where a reasonable fit to the actual spectrum might be obtainable, and it has the nice feature that the electron energy distribution retains the injected form without much softening, which greatly simplifies the analysis.

3.1.2. Parameter Variations on the Unique Solution

In this subsection, we explore how sensitive the above results are to parameter variations. The parameter we want to emphasize is the ratio η of the SSC component to the synchrotron component. From equations (6) and (9), and holding other parameters unchanged, we can see that

$$\eta \propto \mathcal{D}^{-8} \propto B^{-8} \quad , \quad (16)$$

which implies that a small change in magnetic field and/or Doppler factor could result in a large variation in η . Figure 4 shows this effect when B is being varied. The general trend from

equation (16) is indeed confirmed, i.e., smaller/larger B (versus B_s) gives much larger/smaller η . For $B < B_s$, the variation amplitude in η does not exactly follow equation (16). We attribute this discrepancy mostly to variation in f_c because both γ_{\max} and synchrotron photon energy in comoving frame are varying for different B . Additionally, when $\eta > 1$ (SSC cooling is more important than synchrotron cooling), electron distribution is subject to stronger cooling. This is evident in its rapid spectral variation in the middle panel of Figure 4. For larger B which results in $\eta < 1$, equation (16) is mostly confirmed. Note that the Doppler factor \mathcal{D} , using equation (6), is now getting uncomfortably large.

To conclude, in the limit that the cooling time of the highest energy electrons is longer than the dynamic timescale on which injection occurs, we can most likely find a *unique* set of parameters that roughly satisfy the observational constraints. The most important prediction is that even though the fluxes of the synchrotron and SSC peaks can vary by a large factor (> 10) in a short time whose time histories look like “pulses”, the duration of emission at other wave bands (such as GeV, MeV, eV) can be considerably longer by at least a factor of 4, which is commensurate with long electron cooling time at those energies.

This parameter space has some interesting implications for interpreting multiwavelength data from blazar monitoring campaigns. Using keV and eV bands as an example (similar arguments can be made for TeV and GeV bands too), since the lifetimes for keV-producing and eV-producing electrons are different, there is really no reason to expect their light curves to track each other and to have the same rise and fall patterns or timescales. Furthermore, when there are multiple injections occurring over a timescale shorter than the lifetime of keV-producing electrons but longer than the lifetime of eV-producing electrons, fluxes at keV could vary rapidly to reflect the multiple injections. Fluxes at eV, however, might only show a continuous increase with no obvious decline because of the accumulation of eV-producing electrons from multiple injections (see also §3.2.5).

3.2. Short Cooling Time Limit

In this subsection we explore the limit where $t_{\text{cool}}(\gamma_{\max}) < t_{\text{dyn}}$, i.e., electrons are efficiently being cooled while they are injected into the system. All the runs in this section have size $R = 1.5 \times 10^{16}$ cm which gives a comoving dynamic timescale $R/c = 5 \times 10^5$ sec, particle’s $\gamma_{\min} = 10$, $\gamma_{\max} = 10^6$, and index $p = 2$. The Doppler factor is chosen as 10 and magnetic field $B = 0.1$ G, though most of the conclusions depend weakly on \mathcal{D} and B in this section. The particularly attractive feature of this limit is that it is possible to achieve short time variabilities for many wave bands, contrary to the case shown in Figure 2 from the previous section.

One serious problem in comparing the theoretical results with the actual observations is that most observations need to accumulate over certain time interval (to collect enough photons) and different integration times are needed for different energy bands. So, in order to make a direct

comparison with the observations, properly averaged fluxes are needed, rather than the prompt flux we have presented above. This inevitably introduces many more additional parameters in determining how photons at different energy bands are sampled. To avoid these complications, as before, we will continue to present the prompt flux results, leaving the problem of integrated fluxes to future studies on detailed spectral fitting of particular sources.

To quantify the relative importance of SSC versus synchrotron, the previous expression for η has to be modified. To recapitulate, the comoving synchrotron photon energy-density is $U_{\text{syn}} \simeq [m_e c^2 / (4\pi R^2 c)] \int_{\gamma_{\text{min}}}^{\gamma_{\text{max}}} N_e(\gamma) |\dot{\gamma}| d\gamma$, where the electron energy loss-rate through synchrotron radiation is given by $\dot{\gamma} = -[4\sigma_{\text{T}} / (3m_e c)] U_B \gamma^2$. Thus, we get

$$\eta = f_c \frac{U_{\text{syn}}}{U_B} = f_c \frac{\sigma_{\text{T}}}{3\pi R^2} \frac{\mathcal{E}}{m_e c^2} \frac{2-p}{3-p} \frac{\gamma_{\text{max}}^{3-p} - \gamma_{\text{min}}^{3-p}}{\gamma_{\text{max}}^{2-p} - \gamma_{\text{min}}^{2-p}} \approx f_c \frac{\sigma_{\text{T}}}{3\pi R^2} \frac{\mathcal{E}}{m_e c^2} \frac{\gamma_{\text{max}}}{\ln(\gamma_{\text{max}}/\gamma_{\text{min}})}, \quad (17)$$

where the last expression applies to the case $p = 2$. On the other hand, if $t_{\text{dyn}} > t_{\text{cool}}$, a cooled electron distribution has to be used when calculating the synchrotron photon energy-density. A very rough estimate of the electron break energy γ_{br} , beyond which cooling dominates can be given as

$$\frac{6\pi m_e c}{\sigma_{\text{T}}} \frac{1}{\gamma_{\text{br}} B^2} \approx \max(t_{\text{inj}}, t_{\text{dyn}}) .$$

The cooled electron distribution has the original index $-p$ between γ_{min} and γ_{br} , and roughly $-p - 1$ between γ_{br} and γ_{max} . Since the number density of electron at high energy end is very small for $p > 1$, the previous expression for N_0 (§3.1.1) still applies. Then we can derive another expression for η as

$$\eta_c = f_c \frac{\sigma_{\text{T}}}{3\pi R^2} \frac{\mathcal{E}}{m_e c^2} \left[\left(\frac{2-p}{3-p} \right) \frac{\gamma_{\text{br}}^{3-p}}{\gamma_{\text{max}}^{2-p}} + 1 \right] \approx f_c \frac{\sigma_{\text{T}}}{3\pi R^2} \frac{\mathcal{E}}{m_e c^2} \left[\frac{\gamma_{\text{br}} + \ln(\gamma_{\text{max}}/\gamma_{\text{br}})}{\ln(\gamma_{\text{max}}/\gamma_{\text{min}})} \right], \quad (18)$$

where again, the last expression applies to the case $p = 2$. Note that this ratio η_c depends on B through γ_{br} . Using the same parameters given previously, we find that equations (17) and (18) give $\eta_c \simeq (\gamma_{\text{br}}/\gamma_{\text{max}})\eta$. In other words, in order to reach the same relative ratio between synchrotron and SSC, more energy is needed (by a factor of $\gamma_{\text{max}}/\gamma_{\text{br}}$ for $p = 2$) if electrons are cooled efficiently during injection.

3.2.1. Dynamics of a Single Injection

In this subsection we concentrate on the dynamics of a single injection event lasting t_{inj} and its corresponding evolution of electron and photon distributions. The idea is to mimic individual flaring events in blazars and gain some basic knowledge of how synchrotron and SSC components are dynamically linked. To simplify the calculations and analysis, we choose 6 total injection energies with a factor of 10 increase from 10^{44} ergs to 10^{49} ergs. These energies in nonthermal electrons are injected over a comoving timescale of $t_{\text{inj}} = 2t_{\text{dyn}}$. We solve equations (1) and (2)

simultaneously and follow the evolution until $10t_{\text{dyn}}$. Electrons are not allowed to escape. With these parameters, $t_{\text{cool}}(\gamma_{\text{max}})$ is much smaller than t_{dyn} , so electrons are appreciably cooled during injection.

Figure 5 shows the νF_ν spectra of these 6 injections taken at $t = t_{\text{inj}}$ and with fluxes divided by $\mathcal{E}/10^{44}$. It is evident that synchrotron is the dominant cooling process for $\mathcal{E} \leq 10^{47}$ cases, whereas SSC becomes the dominant cooling process as the photon energy density builds up in the 10^{48} and 10^{49} cases. In fact, electron cooling is so significant in the 10^{49} case that the maximum synchrotron flux is reduced by almost a factor of 10 compared to other lower injection energy cases, and its SSC peak energy is also much softer than others.

As given in equation (18), the ratio of SSC to synchrotron is roughly proportional to \mathcal{E} . Thus as \mathcal{E} increases, so is this ratio. This is shown as the (almost) linear increase in the SSC peaks of Figure 5. So we conclude that so long as the peak in SSC is less than synchrotron, the magnitude of increase in SSC peak will be the *square* of the magnitude of increase in synchrotron peak. When the SSC component becomes comparable to synchrotron component, the system becomes highly nonlinear, the estimate of γ_{br} based on pure synchrotron cooling is no longer valid, even though equation (18) probably still applies as long as a cooled electron distribution is used.

A further point regarding the relative ratio of SSC versus synchrotron components is that the initial ~ 10 GeV – TeV production via SSC is in the KN regime, which reduces the SSC flux. This implies that an even larger \mathcal{E} is needed than those given in equation (18). Observations of Mrk 421 and 501 seem to indicate roughly the same heights of synchrotron and SSC peaks. Thus, in modeling the time-dependent (or even steady state) emissions from these objects, a full KN cross section has to be used, as was done here in our code.

3.2.2. Dynamics and Light Curves

We now study in detail the full time evolution of three injection cases: $\mathcal{E} = 10^{44}, 5 \times 10^{47}$, and 10^{49} ergs. They are shown in Figures 6, 7, and 8, where the time-evolution of electron distributions and photon spectra are presented. Figures 9, 10, and 11 show the corresponding light curves of different photon energies for the above three injection cases. To qualitatively understand the light curves, we refer to equation (15) again. The peak of the light curves is reached when the production and escape are balanced, which depends on whether particle distribution has softened enough. Furthermore, once the production at certain photon energy has stopped, the pure escape process will produce an exponential decay. Since the photon escape timescale is $t_{\text{dyn}} = R/c$, one could get an estimate of the size by fitting the decline portion of the light curves. This can be done using Figures 9, 10, and 11 where fluxes have been plotted in logarithm. The straight lines give a clear representation of photon escape, especially when it shows up in several energy bands, thus this might be a useful method in analyzing the real blazar data.

3.2.3. Spectral Variations

The flux changes depicted in the above subsection are accompanied by large spectral variations too as shown in Figures 6, 7, and 8. These curves contain a wealth of information, some of which are rather parameter dependent. Nevertheless, we can draw some general conclusions:

(1) Since the cooling time at γ_{\max} is the shortest timescale in our system, the electron distribution at high energy end is always substantially softened. Furthermore, the production of photons $>$ tens of GeV is always in the KN regime using SSC model. Both effects make the TeV spectrum very soft, with a large curvature. [Additional effects such as intrinsic absorption at the source or intergalactic absorption by infrared background can cause further curvature (e.g., Coppi & Aharonian 1999).] This curvature is not consistent with the TeV spectra we have seen from Mrk 421 (Krennrich et al. 1999), but it is perhaps consistent with the observations of Mrk 501 where a curvature in the Compton component is clearly seen (Djannati-Atai et al. 1999).

(2) The “hysteresis” in the relation of photon energy flux and spectral index was first pointed out by Takahashi et al. (1996) at the keV band. In Figures 12, 13, and 14, we show the evolution of photon index as a function of energy flux in the observer’s frame. Clockwise rotation is always seen at 1 GeV, regardless of whether synchrotron or SSC cooling dominates. Clockwise rotation is found at 2 keV for the case where synchrotron losses dominate the electron cooling ($\mathcal{E} = 10^{44}$ ergs). We find that this clockwise rotation at 2 keV is true for all cases with injection energy less than 10^{48} ergs (with the above injection form). This is mostly related to the fact that if we can associate 2 keV with the synchrotron peak, the spectrum always softens when its flux is decreasing because the electrons that can produce 2 keV photons have diminished. When the injection energy is large, the SSC loss is dominant ($\mathcal{E} = 10^{49}$ ergs), the hysteresis diagrams rotate in the opposite sense at 2 keV. The hardening at later time is actually due to the fact that 2 keV flux is now from the first generation of SSC, not synchrotron anymore. Different behaviors of the hysteresis, however, are found at 100 keV: counter-clockwise for $\mathcal{E} = 10^{44}$ ergs and clockwise for $\mathcal{E} = 10^{49}$ ergs. Given these large variations and their sensitivity of various parameters, it is difficult to use these “hysteresis” diagrams to draw firm conclusions.

(3) If observations show a synchrotron peak in 1 – 10 keV band, one should be very careful with fitting the spectrum in the 100 keV energy band (such as OSSE and BeppoSAX), since it is right in the region where synchrotron and SSC meet. There is a very large and rapid spectral evolution during the flare (e.g., Figure 13).

(4) In the rising part of the νF_ν spectra, such as 1 – 10 eV and MeV – GeV, the spectral index variation is much slower than the keV and TeV energy bands even though their fluxes vary by a large factor (e.g., Figures 12, 13, and 14).

(5) To further quantify the spectral evolution, we plot the peak energies of synchrotron and SSC components in νF_ν as a function of time in Figure 15 for the case with $\mathcal{E} = 5 \times 10^{47}$ ergs. An important part is the early softening stage, where the synchrotron peak energy decreases as γ^2

whereas the SSC peak energy goes down first as γ because the scattering is in the KN regime. This effect might be observable with the current keV and TeV observational capabilities. Such a “correlated” evolution in peak energies might provide a definitive test of SSC.

(6) As shown in Figure 5, when the SSC cooling becomes comparable to or dominant over the synchrotron cooling, the synchrotron peak becomes broader than those dominated by synchrotron cooling only.

Some of the above conclusions might be testable using the current data collected on blazars, and some might require much higher quality data.

3.2.4. Time-Dependent Injection

In this subsection we show how different injection profiles change the light curves in a single injection event. Different from the previous subsection where a constant injection is used (box-shaped injection), we calculate another case with a linearly increasing injection rate (triangle-shaped injection), i.e., $Q(\gamma) = Q_0\gamma^{-2}t/t_{\text{dyn}}$ for $0 \leq t \leq 2t_{\text{dyn}}$, and $Q(\gamma) = 0$ for $t > 2t_{\text{dyn}}$. The time evolution is followed until $t = 10t_{\text{dyn}}$ and electrons are allowed to escape with $t_{e,\text{esc}} = 5t_{\text{dyn}}$. We use the same number of particles and same amount of total injected energy in both box- and triangle-shaped injections; the injected energy is 5×10^{47} ergs per $2t_{\text{dyn}}$ in the blob frame. In Figure 16, we compare their light curves at 1 keV. The light curve for the box-shaped injection is asymmetric, because more electrons are injected at an early stage than in the triangle injection. On the other hand, the light curve from triangle injection shape is almost symmetric. In both cases, light curves decay exponentially after the end of the injection.

3.2.5. Multiple Injections

We now move to study other injection profiles, which are done by artificially turning the electron source term on and off. This is admittedly quite artificial. The purpose is to understand whether there are any generic features associated with these multiple injections, which might aid us on modeling the multiple flares often observed from blazars. In all the following runs, we allow electrons to escape with $t_{e,\text{esc}} = 5t_{\text{dyn}}$. Other parameters are the same as the single injection case.

Successive flares can be produced by repeated injections of nonthermal electrons. As an example of this picture, we present light curves for two repeated injection cases of nonthermal electrons. The top panels of Figures 17 and 18 show the injection profiles, which consist of two triangle injections separated by a long ($8t_{\text{dyn}}$) and a short ($2t_{\text{dyn}}$) intervals (in the comoving frame), respectively. In both cases 5×10^{47} ergs are injected in each “flare” with a triangle-shaped time profile. The lower panels of Figures 17 and 18 show the expected light curves calculated by our code. The shape of the light curves from each injection is very similar to that in Figure 16 where

a single injection is involved (i.e., quasi-symmetric). The peak fluxes of light curves in multiple injections are, however, affected by the separation time of two flares. When the separation interval is longer than the electron escape time ($5t_{\text{dyn}}$), the light curves can almost be regarded as a simple sequence of two separate single injections. But when the separation interval is shorter than the electron escape time, multiwavelength light curves become rather complicated. The main physical reason behind this complication is the dynamic accumulation of both photons and relativistic electrons. First of all, 1 eV and 1 keV emissions are from synchrotron and others are from SSC. All the SSC emissions have second peak higher than the first one, this is due to the increase both in soft photon energy density and in the number of electrons which are not completely cooled yet when the second injection occurs. This accumulation of electrons also accounts for the increase in 1 eV synchrotron flux. The 1 keV emissions, however, show a lower flux in the second peak, this is because the relativistic electrons from the second injection are subject to a much stronger cooling due to the enhanced photon energy density from the first injection. In addition to the flux differences, there are obvious delays in reaching the peak fluxes for different wavelengths with respect to the synchrotron and SSC peaks, though 1 keV and 1 TeV fluxes track each other rather well.

As demonstrated in these figures, the slow response and relatively small amplitude variations at the photon energies other than the synchrotron and SSC peaks argue against the usual belief of closely correlated variations in multiwavelength observations. Only the emissions from the tail of the electron energy distribution can be reliably used as diagnostics for separate injections. Still, extra caution is obviously needed when relating the energy contained in nonthermal particles versus the observed fluxes.

4. SUMMARY AND DISCUSSIONS

Using a homogeneous synchrotron self-Compton model, we have calculated the time evolution of emission spectra and electron energy distributions when nonthermal electrons are uniformly injected into a relativistically moving plasma blob with constant velocity. We have found that:

(1) When the luminosities of the synchrotron and SSC peaks are comparable, the electron cooling by inverse Compton scattering is not negligible and the system is inherently nonlinear and dynamic. One has to solve the time-dependent, coupled electron and photon kinetic-equations self-consistently. Furthermore, since observations are most sensitive to the peak fluxes of synchrotron and SSC components, accurate treatments of synchrotron emissivity due to the end point effects and inverse Compton scattering in the KN regime are quite essential.

(2) When the cooling time at the maximum particle energy is longer than the injection timescale ($\geq R/c$), the light curve of emissions corresponding to the tail of the electron distribution can have short, large amplitude variations but emissions at other wavelengths show considerably longer and smaller amplitude changes. Additionally, spectral evolution is also rather slow. All

these features are simply caused by the long cooling time of electrons.

(3) When cooling time at the maximum particle energy is shorter than the dynamic timescale, strong spectral evolutions are observed for both synchrotron and SSC components and short duration flares are obtained in most energy bands.

(4) Generally, the prompt TeV spectrum is curved due to the KN effect and the fact that TeV-production electrons are usually in a cooled distribution. This consideration does not take into account the possible infrared background attenuation of the TeVs, which might cause further curvature in the TeV spectrum. On the other hand, most current TeV observations require an accumulation time probably much longer than the dynamic timescale of the blob, so that it might still be possible to obtain a quasi power-law TeV spectrum by averaging over an evolving spectrum. Further study is needed to address this issue.

(5) We recommend plotting the light curves in a fashion that is logarithmic flux versus linear time. The goal is to look for exponential decays at specific energy bands, which might give direct measurements of the size of the system, as indicated in Figures 9 – 11.

(6) One has to be cautious about the common belief that light curves in different energy bands should track each other. The electrons responsible for producing specific energy photons might have quite different lifetimes, especially when multiple and closely spaced injections are involved. This complication also applies to the leading/lagging analysis for different photon energy bands.

(7) When high time-resolution spectroscopy is available both in keV and TeV bands, one should be able to prove whether TeV production is via SSC process by comparing the rates of spectral softening as done in Figure 15.

The primary purpose of this paper is to investigate the radiative signatures in a purely cooling and dynamic system, thus providing a bridge between observations and the detailed but largely unknown physics of particle energization processes. Since we did not address the particle acceleration problem here, in this sense, some of the conclusions drawn above are certainly subject to revisions as our understanding of energy flow in AGNs improves.

In conclusion, we have found that solving time-dependent, coupled electron and photon kinetic-equations provides an easy and efficient way of comparing multiwavelength, time-dependent observations with some simplified SSC models. It has the advantage of naturally combining the spectral and temporal evolutions in a dynamic system, which is very useful when more and more high quality data become available.

We thank C. Dermer for useful discussions and the anonymous referee for the helpful comments. H.L. gratefully acknowledges the support of an Oppenheimer Fellowship, and his research is supported by the Department of Energy, under contract W-7405-ENG-36. M.K. thanks F. Takahara for stimulating discussions and his research was partially supported by Scientific Research Grants (09223219, 10117215) from the Ministry of Education, Science, Sports and

Culture of Japan.

REFERENCES

- Blandford, R.D., & Rees, M.J. 1978, in Pittsburgh Conf. on BL Lac Objects, ed. A.M. Wolfe (Pittsburgh: Univ. Pittsburgh Press), 328
- Bloom, S. D., & Marscher, A. P. 1996, ApJ, 461, 657
- Böttcher, M., Mause, H., & Schlickeiser, R. 1997, A&A, 324, 395
- Buckley, J. H. et al. 1996, ApJ, 472, L9
- Catanese, M. et al. 1997, ApJ, 487, L143
- Coppi, P. S., & Aharonian, F. A. 1999, ApJ, 521, L33
- Coppi, P. S., & Blandford, R. D. 1990, MNRAS, 245, 453
- Crusius, A., & Schlickeiser, R. 1986, A&A, 164, L16
- Dermer, C. D. 1998, ApJ, 501, L157
- Dermer, C. D., Sturmer, S. J., & Schlickeriser, R. 1997, ApJS, 109, 103
- Djannati-Atai, A. et al. 1999, A&A, submitted
- Georganopoulos, M., & Marcher, A. P. 1998, ApJ, 501, L11
- Ghisellini, G., Guilbert, P. W., & Svensson, R. 1988 ApJ, 334, L5
- Ghisellini, G., & Madau, P. 1996, MNRAS, 280, 67
- Ghisellini, G., Celotti, A., Fossati, G., Maraschi, L., & Comastri, A. 1998, MNRAS, 301, 451
- Inoue, S., & Takahara, F. 1996, ApJ, 463, 555
- Jones, F. C. 1968, Physical Review, 167, 1159
- Kataoka, J. et al. 1999, ApJ, 514, 318
- Kirk, J. G., Rieger, F. M., & Mastichiadis, A. 1998, A&A, 333, 452
- Krennrich, F. et al. 1999, ApJ, 511, 149
- Kusunose, M., Coppi, P.S., & Li, H. 1999, unpublished, available upon request
- Macomb, D. J., et al. 1995, ApJ, 449, L99

- Macomb, D. J., et al. 1996, ApJ, 459, L111 (erratum)
- Mastichiadis, A., & Kirk, J. G. 1997, A&A, 320,19
- Pian, E. et al. 1998, ApJ, 492, L17
- Robinson, P. A., & Melrose, D. B. 1984, Australian J. Physics, 37, 675
- Romanova, M.M. & Lovelace, R.V.E. 1997, ApJ, 475, 97
- Sikora, M., Madejski, G., Moderski, R., Poutanen, J. 1997, ApJ, 484, 108
- Takahashi, T., Tashiro, M., Madejski, G., Kubo, H., Kamae, T., Kataoka, J., Kii, T., Makino, F.,
Makishima, K., & Yamasaki, N. 1996, ApJ, 470, L89
- Vermeulen, R.C. & Cohen, M.H. 1994, ApJ, 430, 467
- von Montigny, C. et al. 1995, ApJ, 440, 525

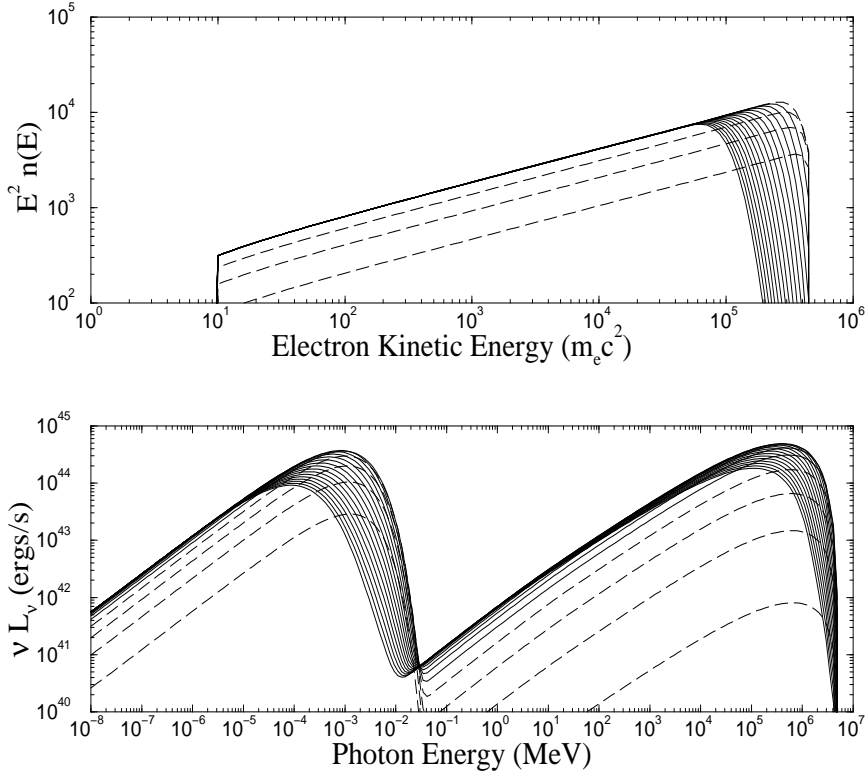


Fig. 1.— Time evolution of electron energy distribution (upper panel) and the corresponding photon spectra (lower panel) using parameters from the unique solution discussed in §3.1.1. Electrons are injected at a constant rate lasting $2t_{\text{dyn}}$ in the comoving frame. There are 20 curves in each panel, which start at $t = 0.5t_{\text{dyn}}$ and end at $t = 10t_{\text{dyn}}$ with a time interval of $0.5t_{\text{dyn}}$ between them. The injection process is shown by the dashed curves moving up in $n(E)$, along with the increasing photon fluxes. After the injection stops, electrons are continuously cooled and the photon spectrum softens. These parameters give a comparable peak fluxes for synchrotron and SSC components.

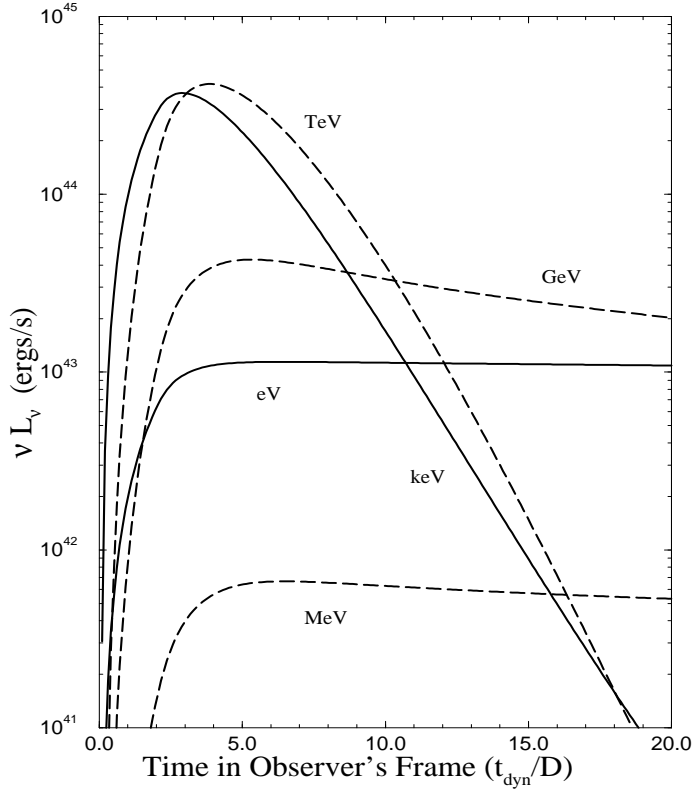


Fig. 2.— Multiwavelength light curves in observer’s frame (\mathcal{D} is assumed to be 10) using parameters from the unique solution (cf. Figure 1). Fluxes at the synchrotron and SSC peaks show fast time variability with large amplitudes, but fluxes at other wavelengths have a very long plateau with very small amplitude variation.

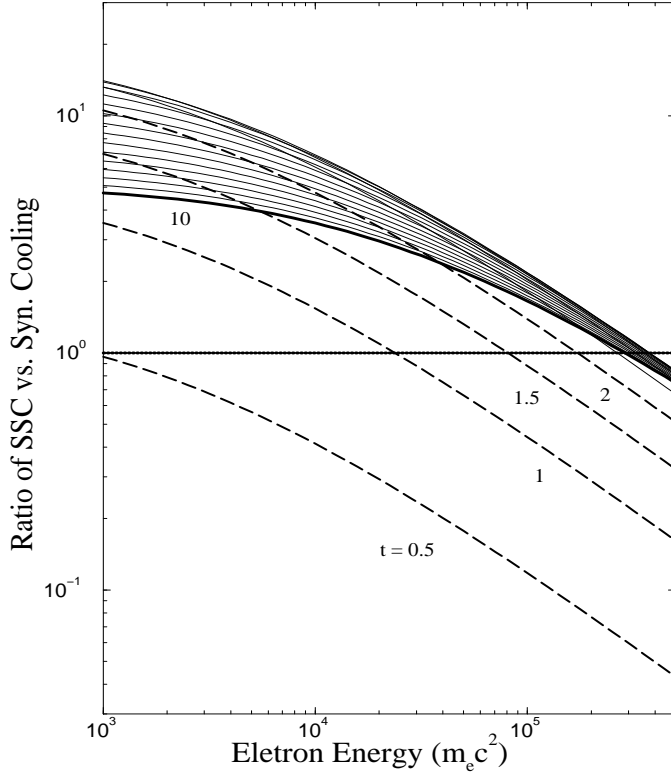


Fig. 3.— Shown is $|\dot{\gamma}_{\text{SSC}}/\dot{\gamma}_{\text{syn}}|$ as a function of electron energy at different times (from $0.5 - 10t_{\text{dyn}}$) using parameters from the unique solution (cf. Figure 1). The horizontal solid line at the ratio being 1 is plotted to guide the comparison. The SSC process becomes important as soon as the photon energy is built up and, in fact, is more important than synchrotron cooling for most of the electron energies.

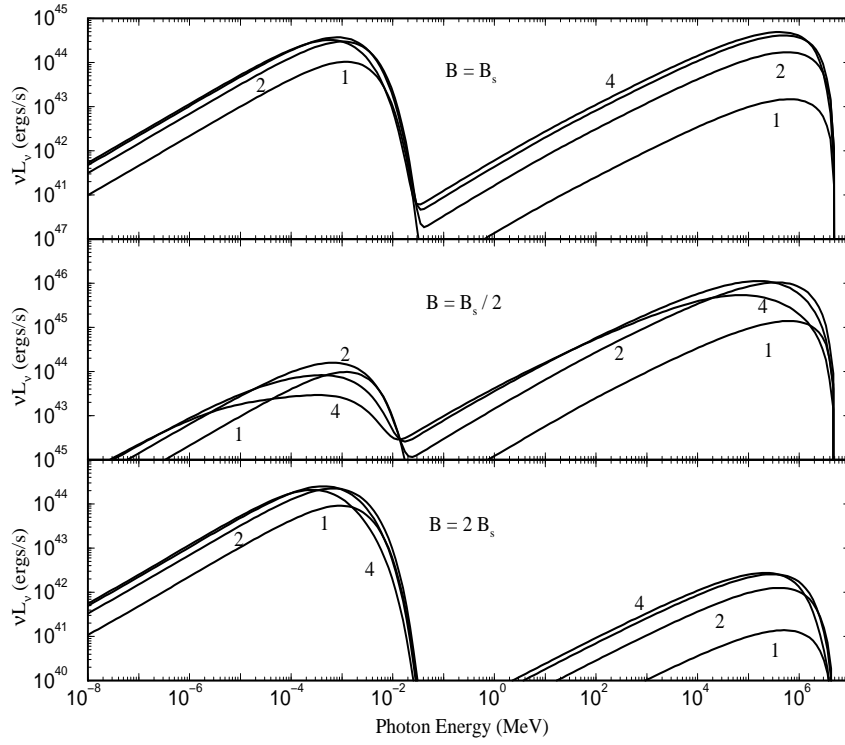


Fig. 4.— Shown is the photon spectral evolution from $0 - 4t_{\text{dyn}}$ as the magnetic field is varied from the unique solution value B_s . The ratio η is unity when $B = B_s$ (cf. Figure 1) but varies nearly as $(B_s/B)^8$ as shown in the middle and lower panels here.

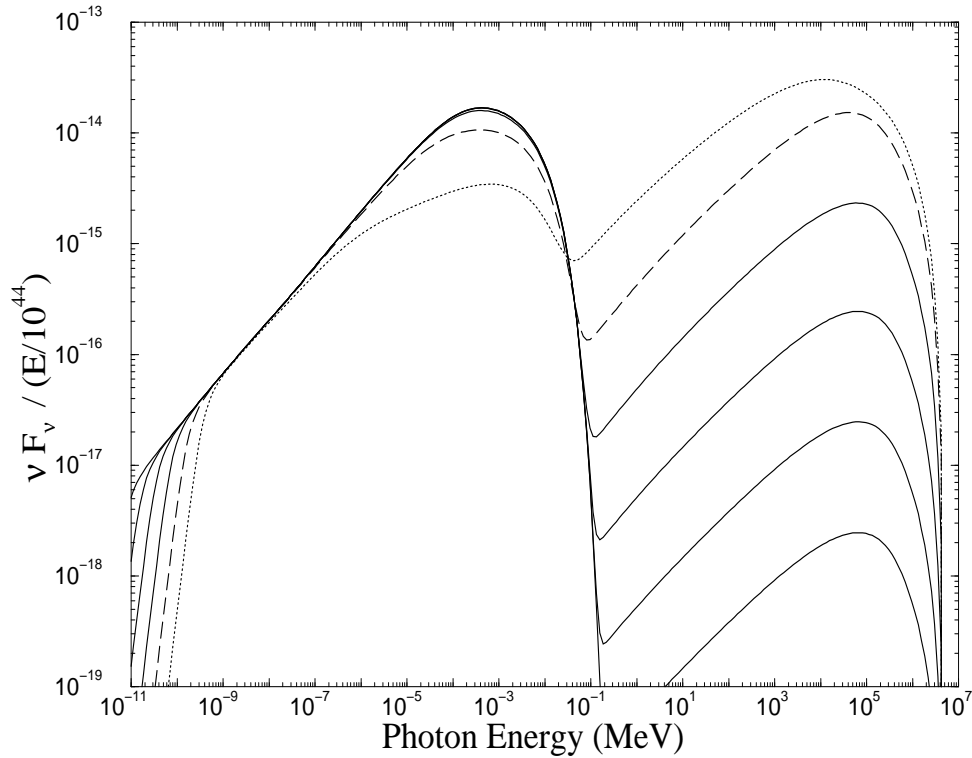


Fig. 5.— The photon spectra νF_ν for 6 different total-injection-energy \mathcal{E} , ranging from 10^{44} ergs to 10^{49} ergs with a factor of 10 increment in each case. All 6 spectra are taken at the end of electron injection ($t = 2t_{\text{dyn}}$) and their fluxes are divided by $\mathcal{E}/10^{44}$ so that if the synchrotron flux was exactly proportional to \mathcal{E} , they would have had the same heights. As \mathcal{E} increases, the electron cooling changes from synchrotron dominated (when $\mathcal{E} \leq 10^{47}$) to synchrotron self-Compton (SSC) dominated. Note that the increase in SSC component is proportional to \mathcal{E}^2 for $\mathcal{E} \leq 10^{47}$. When SSC cooling is very strong, electrons cool so quickly that the synchrotron flux at $2t_{\text{dyn}}$ is no longer scaled as \mathcal{E} anymore as shown in the 10^{48} (*dashed*) and 10^{49} (*dotted*) cases. Also in these large \mathcal{E} cases, the efficient cooling makes the synchrotron peak rather broad.

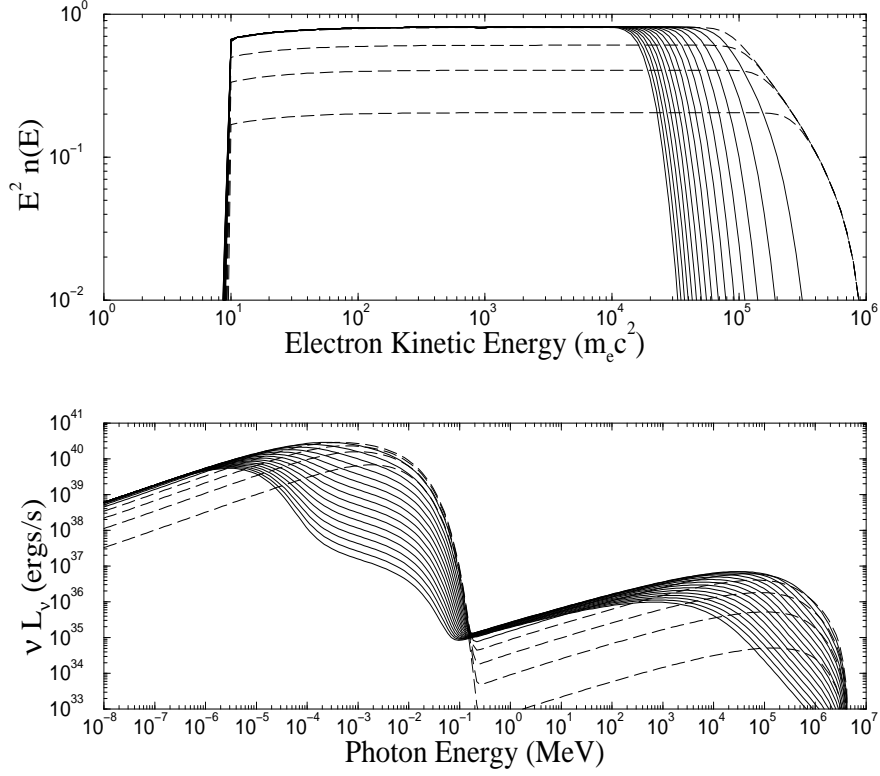


Fig. 6.— Time evolution of electron energy distribution (upper panel) and the corresponding photon spectra (lower panel) for $\mathcal{E} = 10^{44}$ ergs. Electrons are injected at a constant rate lasting $2t_{\text{dyn}}$ in the comoving frame, with $\gamma_{\text{min}} = 10$, $\gamma_{\text{max}} = 10^6$, and index $p = 2$. There are 20 curves in each panel, which start at $t = 0.5t_{\text{dyn}}$ and end at $t = 10t_{\text{dyn}}$ with a time interval of $0.5t_{\text{dyn}}$ between them. The injection process is shown by the dashed curves moving up in $n(E)$, along with the increasing photon fluxes. After the injection stops, electrons are continuously cooled and photon spectrum softens (solid curves). With this injection energy, the SSC peak is considerably lower than the synchrotron peak.

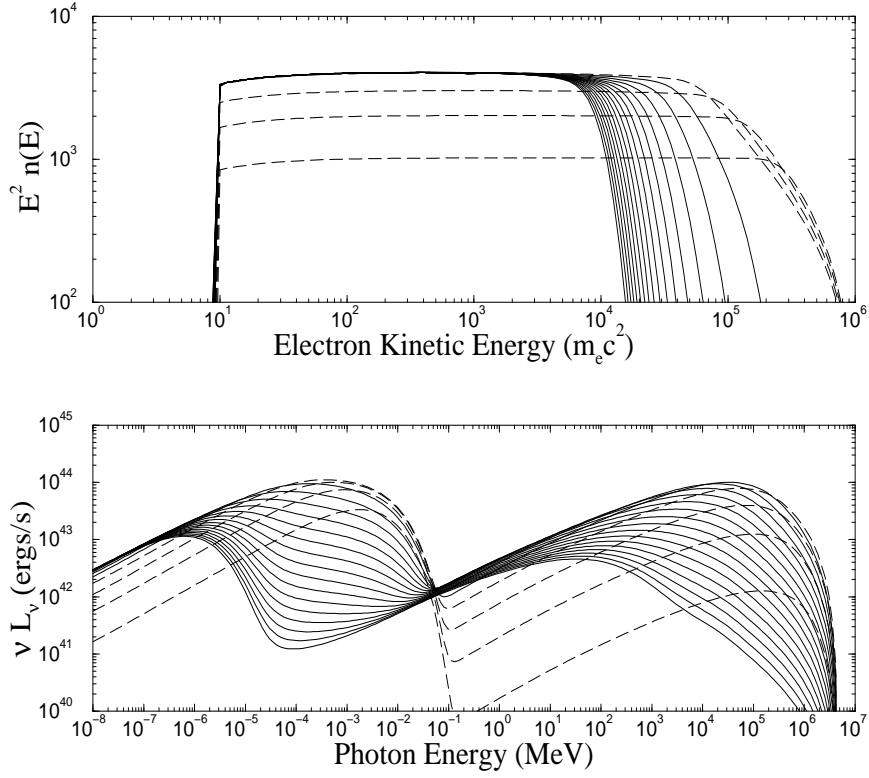


Fig. 7.— Same as Figure 6, except that $\mathcal{E} = 5 \times 10^{47}$ ergs. Now the SSC component has become comparable to the synchrotron component, and the whole system understandably evolves on a faster timescale.

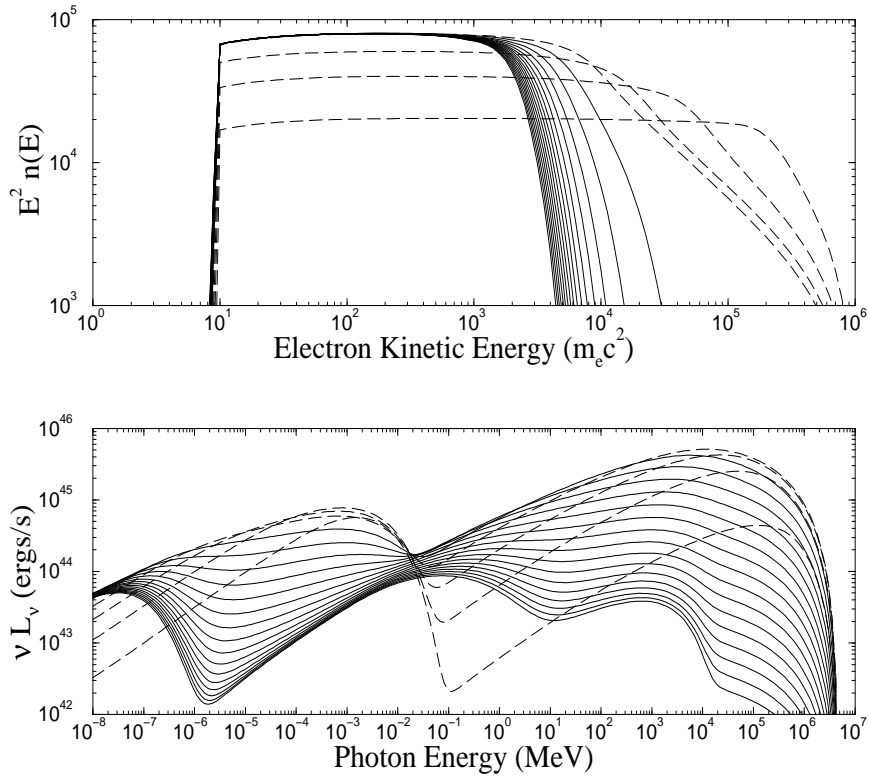


Fig. 8.— Same as Figure 6, except that $\mathcal{E} = 10^{49}$ ergs. The SSC component dominates over the synchrotron component, and the buildup of synchrotron photon energy-density is so quick that electron cooling is very efficient. Towards the end of simulation ($\sim 10t_{\text{dyn}}$), multiple Compton scattering features are evident.

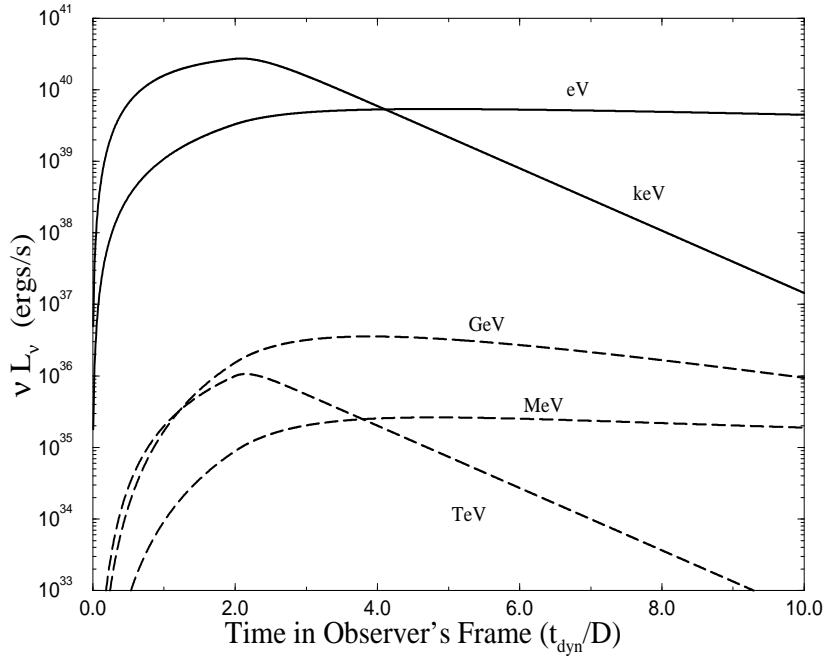


Fig. 9.— Multiwavelength light curves in observer’s frame (\mathcal{D} is assumed to be 10) with $\mathcal{E} = 10^{44}$ ergs (cf. Figure 6). Solid and dashed curves are for synchrotron and SSC components, respectively. The exponential decay depicted by the keV and TeV fluxes allows a direct estimate of the size of the emission cloud.

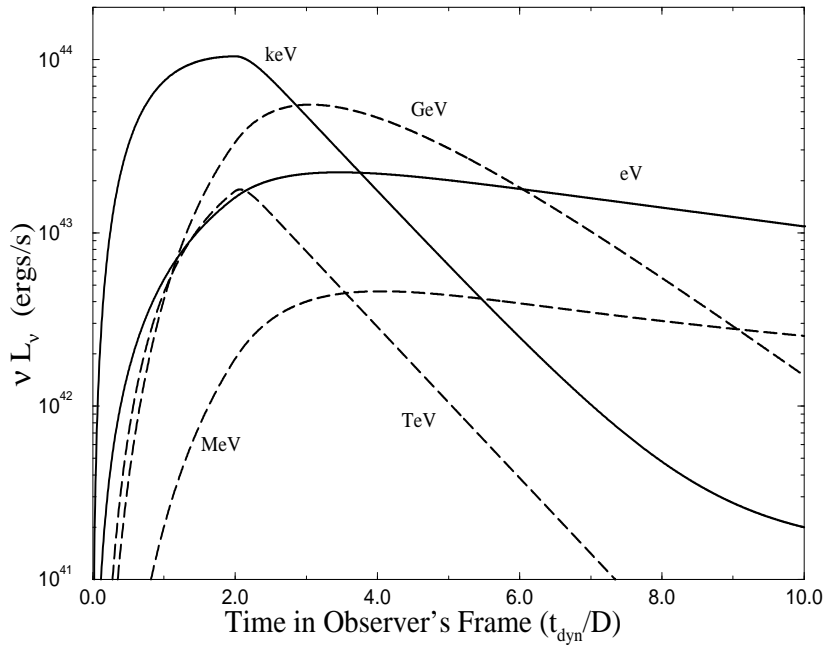


Fig. 10.— Same as Figure 9 except that $\mathcal{E} = 5 \times 10^{47}$ ergs. (Also cf. Figure 7)

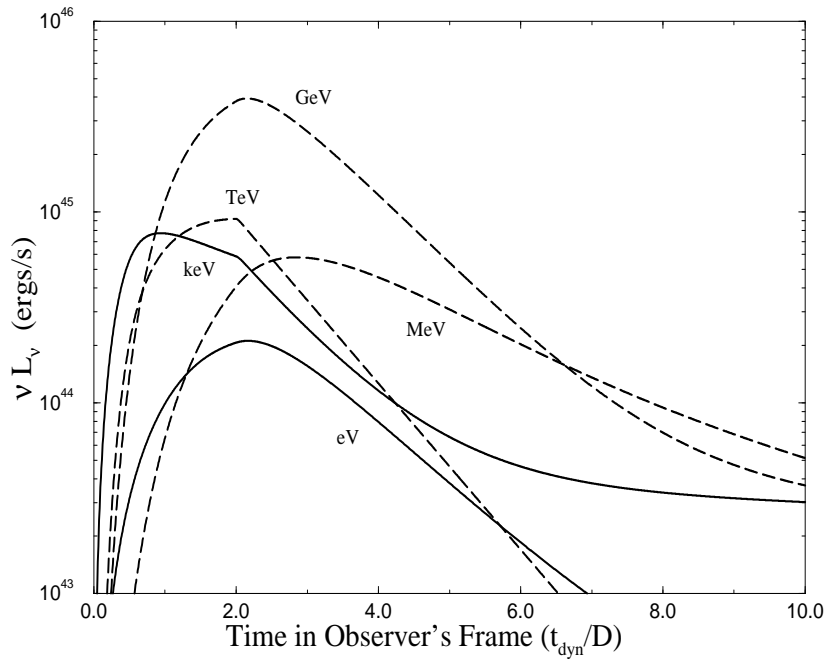


Fig. 11.— Same as Figure 9 except that $\mathcal{E} = 10^{49}$ ergs. (Also cf. Figure 8)

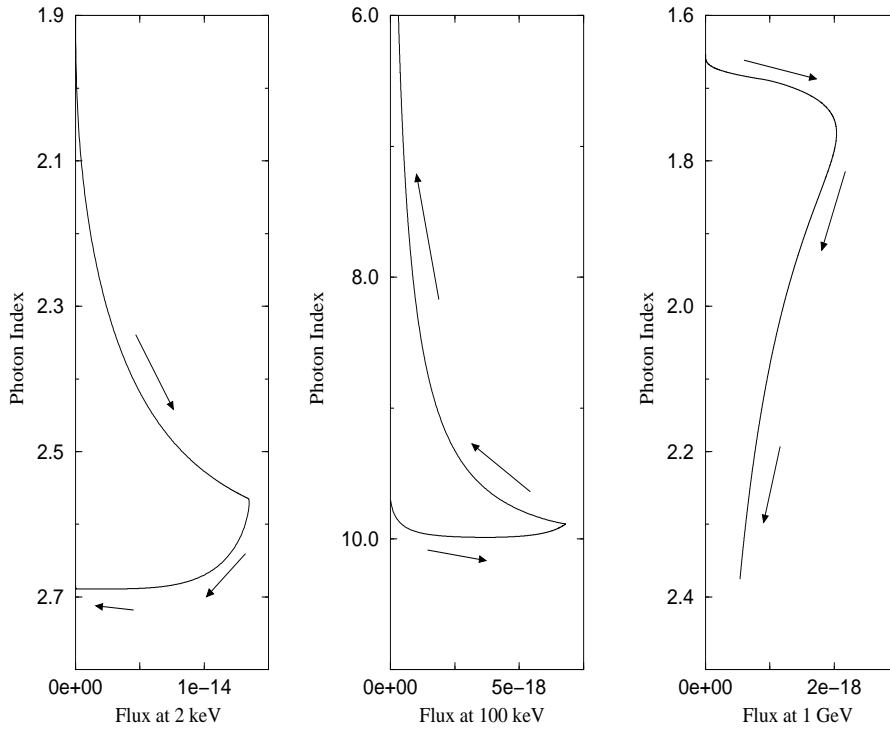


Fig. 12.— The time evolution of the correlation between the photon index and the flux ($\text{ergs cm}^{-2} \text{s}^{-1}$) at 2 keV, 100 keV, and 1 GeV, respectively. Arrows indicate the direction of the time evolution. The total injected energy is $\mathcal{E} = 10^{44}$ ergs. A large spectral evolution is seen at 100 keV, where synchrotron and SSC components mix. Spectral evolution at keV and GeV bands are relatively moderate and clockwise.

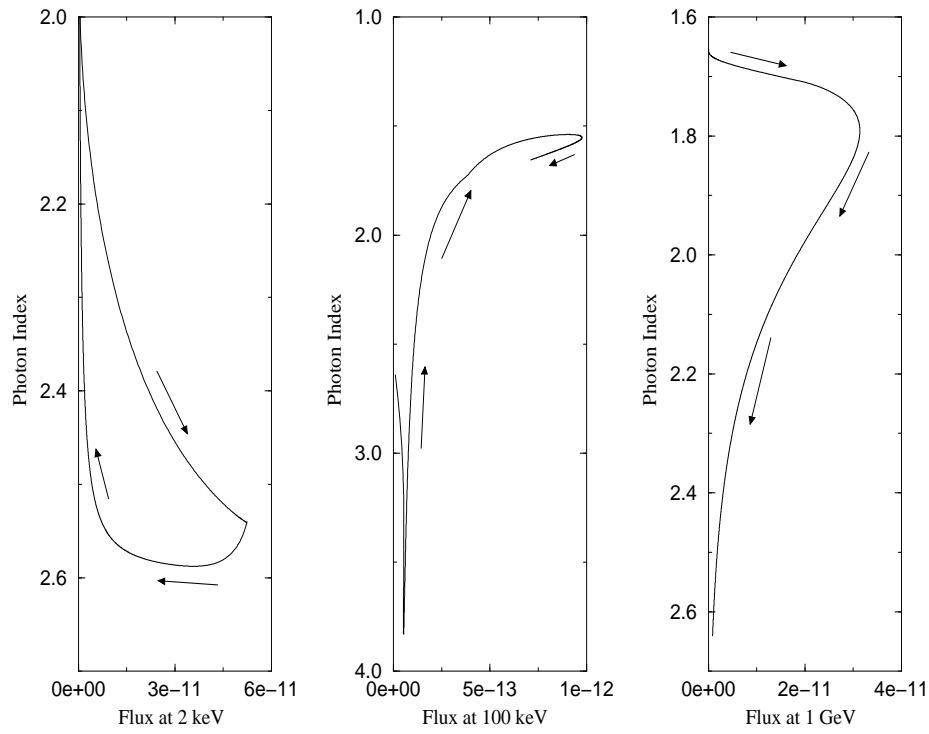


Fig. 13.— Same as Figure 12 except that $\mathcal{E} = 5 \times 10^{47}$ ergs. The evolution is qualitatively the same as in Figure 12.

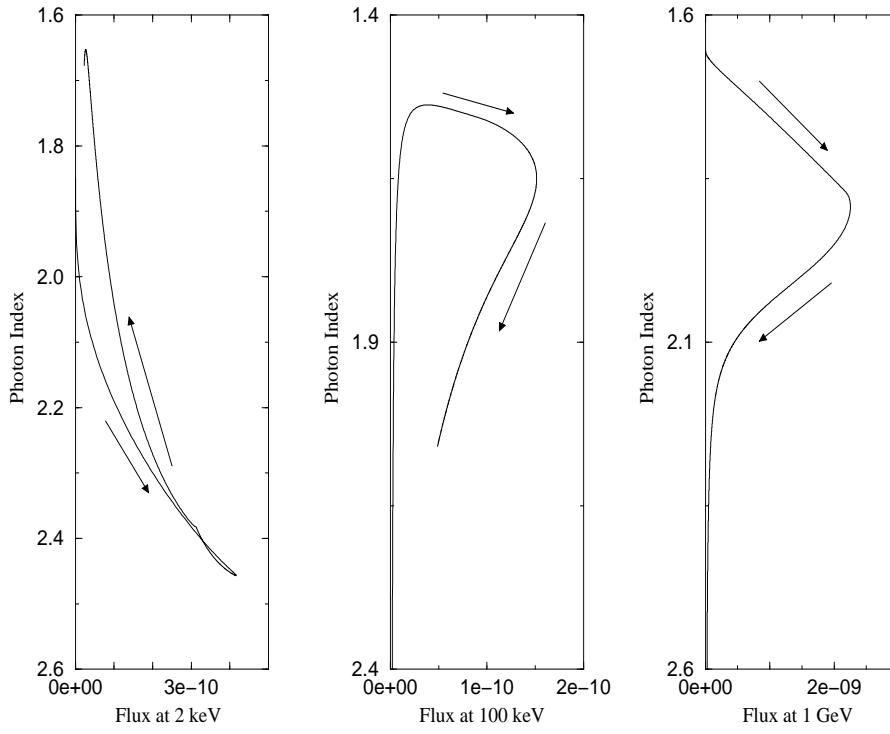


Fig. 14.— Same as Figure 12 except that $\mathcal{E} = 10^{49}$ ergs. Strong evolution at 2 keV is evident, mostly due to the efficient cooling of electrons by SSC process.

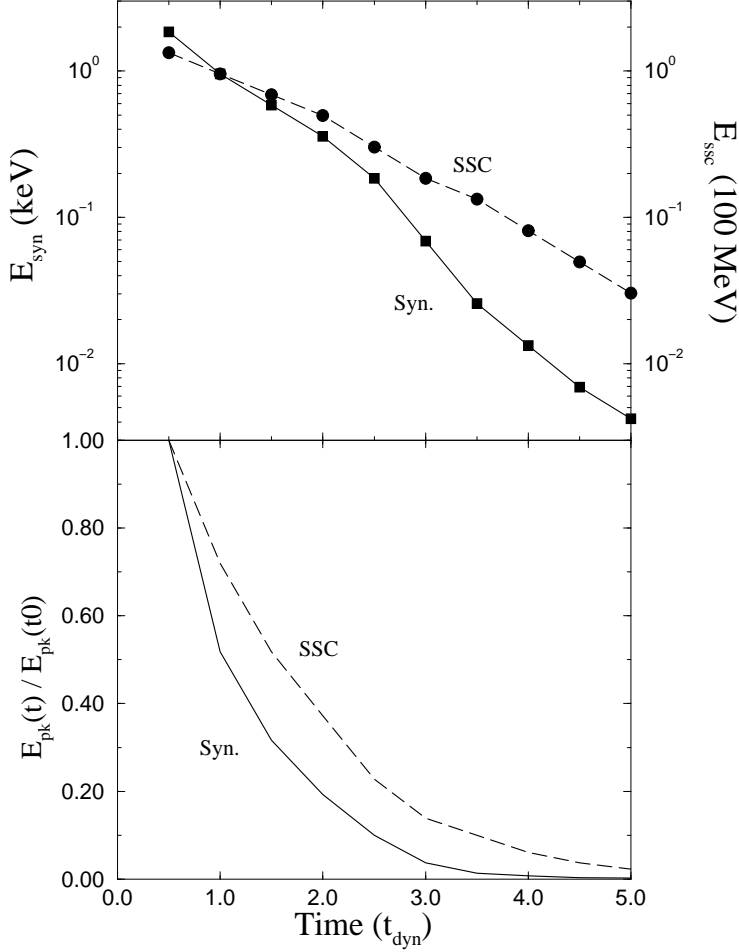


Fig. 15.— Evolution of peak photon energies of both synchrotron and SSC components. The total injected energy is $\mathcal{E} = 5 \times 10^{47}$ ergs (cf. Figure 7). The upper panel shows their actual values and the lower panel shows the normalized values after dividing each peak energy by the value at $t = 0.5t_{\text{dyn}}$ for synchrotron and SSC components, respectively. The synchrotron peak energy ($\propto \gamma^2$) decreases faster than SSC peak energy ($\propto \gamma$) *initially*, because SSC process is still in the Klein-Nishina regime.

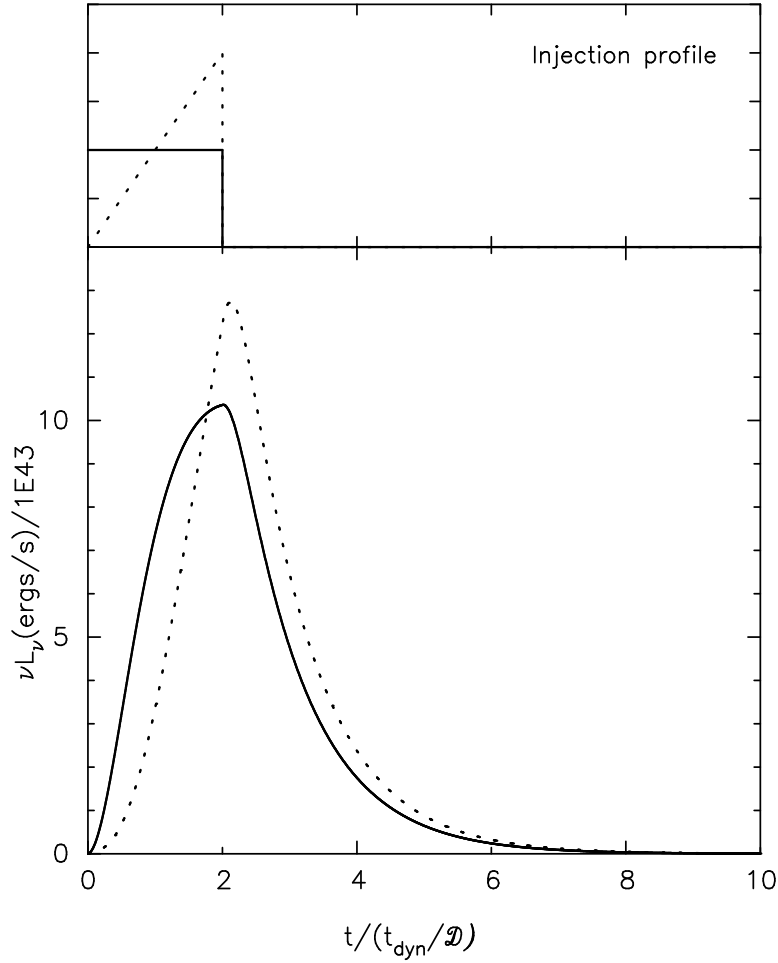


Fig. 16.— Light curves of observed spectra at 1 keV when power-law electrons are injected. Solid curve is calculated when $Q(\gamma) = Q_0\gamma^{-2}$ for $0 \leq t \leq 2t_{\text{dyn}}$, and $Q(\gamma) = 0$ for $t > 2t_{\text{dyn}}$. Dotted curve is obtained when $Q(\gamma) = Q_0\gamma^{-2}t/t_{\text{dyn}}$ for $0 \leq t \leq 2t_{\text{dyn}}$, and $Q(\gamma) = 0$ for $t > 2t_{\text{dyn}}$. The upper panel shows the time profile of the injection Q in arbitrary units.

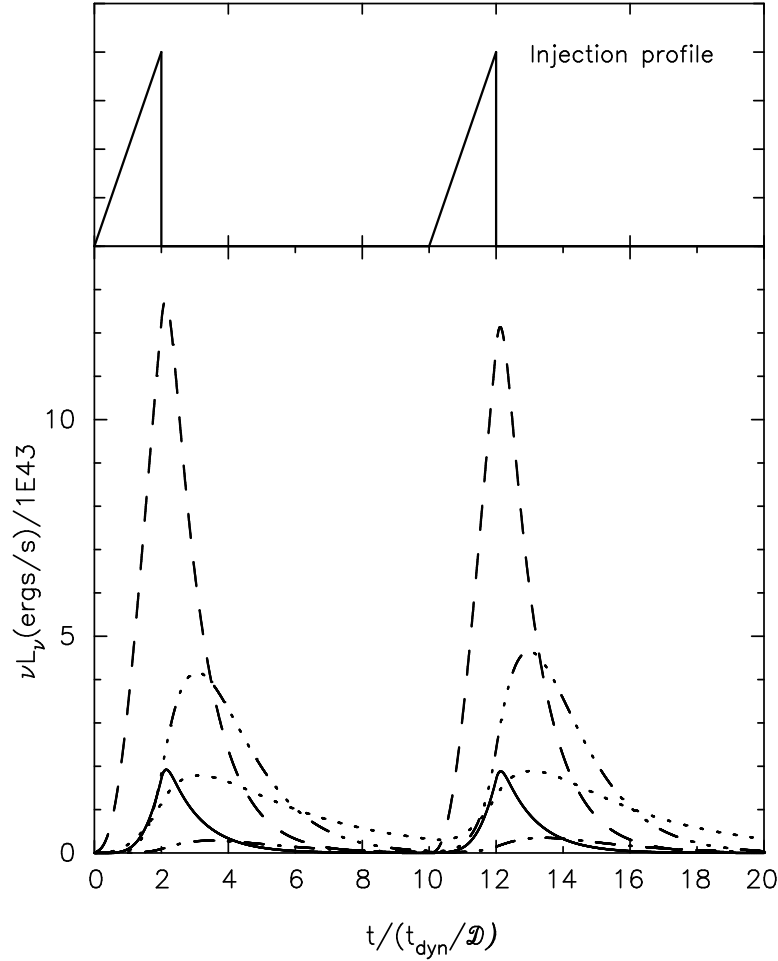


Fig. 17.— Expected light curves at different wavelengths (lower panel) when power-law electrons are injected according to the profile in the upper panel. The time is measured in the observer’s frame. In the comoving frame, two injections are separated by $8t_{\text{dyn}}$, longer than the electron escape timescale, which is chosen as $5t_{\text{dyn}}$. The same amount of energy, 5×10^{47} ergs, is injected in each flare. The dotted, dashed, dash-dotted, dash-dot-dot-dotted, and solid represent fluxes at 1 eV, 1 keV, 1 MeV, 1 GeV, and 1 TeV, respectively. The two flares can be regarded as a simple sequence of two unrelated injections.

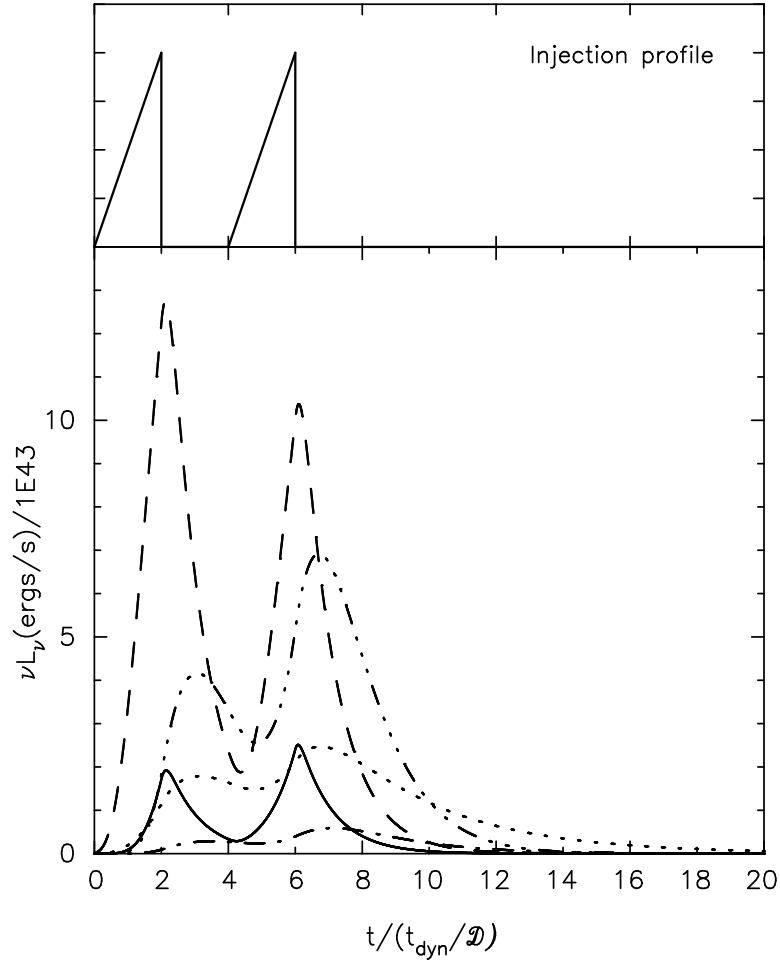


Fig. 18.— Same as Figure 17, except that the separation of two flares is shorter ($2t_{\text{dyn}}$) than the electron escape timescale. The second flare is now strongly affected by the residual effects from the first electron injection.